

# Naval Research Laboratory

Stennis Space Center, MS 39529-5004



NRL/FR/7323--93-9444

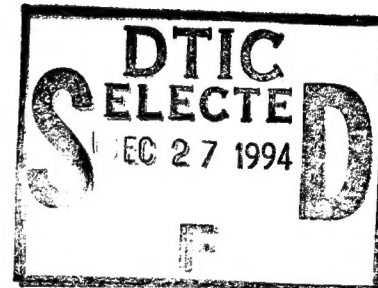
## Hindcasting Wind-Driven Anomalies Using Reduced-Gravity Global Ocean Models with 1/2° and 1/4° Resolution

E. JOSEPH METZGER  
HARLEY E. HURLBURT  
GREGG A. JACOBS  
JOHN C. KINDLE

*Ocean Dynamics and Prediction Branch  
Oceanography Division*

September 30, 1994

"Original contains color  
plates: All DTIC reproductions will be in black and white"



19941219 050

Approved for public release; distribution is unlimited.

DTIC QUALITY INSPECTED 1

# REPORT DOCUMENTATION PAGE

*Form Approved  
OMB No. 0704-0188*

Public reporting burden for this collection of information is estimated to average 1 hour per response, including the time for reviewing instructions, searching existing data sources, gathering and maintaining the data needed, and completing and reviewing the collection of information. Send comments regarding this burden or any other aspect of this collection of information, including suggestions for reducing this burden, to Washington Headquarters Services, Directorate for Information Operations and Reports, 1215 Jefferson Davis Highway, Suite 1204, Arlington, VA 22202-4302, and to the Office of Management and Budget, Paperwork Reduction Project (0704-0188), Washington, DC 20503.

1. AGENCY USE ONLY (Leave blank)	2. REPORT DATE	3. REPORT TYPE AND DATES COVERED	
	September 30, 1994	Final	
4. TITLE AND SUBTITLE Hindcasting Wind-Driven Anomalies Using Reduced-Gravity Global Ocean Models with 1/2° and 1/4° Resolution			5. FUNDING NUMBERS
			Job Order No. 573508904
			Program Element No. 0602435N
			Project No. RM35G93
			Task No. 201
			Accession No. DN251050
6. AUTHOR(S) E. Joseph Metzger, Harley E. Hurlburt, Gregg A. Jacobs, and John C. Kindle			8. PERFORMING ORGANIZATION REPORT NUMBER NRL/FR/7323--93-9444
7. PERFORMING ORGANIZATION NAME(S) AND ADDRESS(ES) Naval Research Laboratory Oceanography Division Stennis Space Center, MS 39529-5004			10. SPONSORING/MONITORING AGENCY REPORT NUMBER
9. SPONSORING/MONITORING AGENCY NAME(S) AND ADDRESS(ES) Office of Naval Research ONR Code 124 800 N. Quincy Street Arlington, VA 22217-5000			11. SUPPLEMENTARY NOTES
12a. DISTRIBUTION/AVAILABILITY STATEMENT Approved for public release; distribution is unlimited.			12b. DISTRIBUTION CODE
13. ABSTRACT (Maximum 200 words)  Global versions of the Navy Layered Ocean Model are used to hindcast wind-driven oceanic anomalies. These versions are reduced-gravity with the lowest layer infinitely deep and at rest. Grid resolutions of 0.5° (1/2°) and 0.25° (1/4°) are used. Winds at the 1000-mbar level from the European Centre for Medium-Range Weather Forecasts are used as forcing functions for the models over the 1981–1990 time frame. The models' ability to reproduce wind-forced anomalies on intraseasonal to interannual time scales is studied by comparing the model solutions with various observational data sets. These include satellite altimetry, drifting buoys, and island/coastal sea-level stations. The effects of varying horizontal and vertical resolution are also investigated.  The models are able to hindcast many of the wind-driven anomalies; the best correlation is found in the tropical regions where the oceanic response to atmospheric forcing is the most rapid. At midlatitudes, mesoscale flow instabilities are a major source of oceanic anomalies. However, the resolution of the global models used here is not adequate for these instabilities. In addition, the reduced-gravity models lack the barotropic mode and the realistic bottom topography, both of which can play an important role in the flow instabilities. A technique that gives maps showing the fraction of variability in the hindcast that is deterministic (in response to atmospheric forcing) and the fraction that is not deterministic (due to flow instabilities) is also demonstrated.			
14. SUBJECT TERMS ocean models, ocean forecasting, fronts (oceanography) air-sea interaction			15. NUMBER OF PAGES 23
			16. PRICE CODE
17. SECURITY CLASSIFICATION OF REPORT Unclassified	18. SECURITY CLASSIFICATION OF THIS PAGE Unclassified	19. SECURITY CLASSIFICATION OF ABSTRACT Unclassified	20. LIMITATION OF ABSTRACT Same as report

## CONTENTS

1.0 INTRODUCTION .....	1
2.0 MODEL DESCRIPTION .....	1
2.1 Atmospheric Forcing .....	2
3.0 MODEL RESPONSE TO LARGE-SCALE FORCING .....	2
4.0 MODEL CLIMATOLOGY .....	4
5.0 WIND FORCING VERSUS FLOW INSTABILITIES .....	7
IN OCEANIC ANOMALY GENERATION	
6.0 UPPER-OCEAN TRAJECTORY FIELDS .....	9
7.0 ISLAND/COASTAL SEA-LEVEL COMPARISON .....	14
8.0 CONCLUSIONS .....	18
9.0 ACKNOWLEDGMENTS .....	19
10.0 REFERENCES .....	19

Accession For	
NTIS	CRA&I <input checked="" type="checkbox"/>
DTIC	TAB <input type="checkbox"/>
Unannounced <input type="checkbox"/>	
Justification .....	
By .....	
Distribution / .....	
Availability Codes .....	
Dist	Avail and/or Special
A-1	

## HINDCASTING WIND-DRIVEN ANOMALIES USING REDUCED-GRAVITY GLOBAL OCEAN MODELS WITH 1/2° AND 1/4° RESOLUTION

### 1.0 INTRODUCTION

Three versions of a global ocean model are used to investigate the ability of wind-driven ocean models to hindcast and to help identify a particular class of wind-forced oceanic anomalies. This work is done by forcing the ocean models using an operational atmospheric wind product and then by comparing the model response to suitable oceanic observations that are contemporaneous with the atmospheric forcing. No assimilation of time-dependent oceanic data is used in the model. As discussed by Hurlburt (1984, 1987), the oceanic anomalies of interest here are a direct integrated response to atmospheric forcing on time scales much longer than the 1-week time scale of atmospheric predictability. Therefore, they are insensitive to errors in depicting the daily fluctuations in the weather, but are sensitive to errors on monthly and interannual time scales. Other studies of this class of anomalies include Haney (1980) for the midlatitude North Pacific, Busalacchi et al. (1983) and Cane et al. (1986) for El Niño and the equatorial Pacific, and Pares-Sierra and O'Brien (1989) for sea level along the west coast of North America.

### 2.0 MODEL DESCRIPTION

The global ocean models used here are reduced-gravity versions of the Navy Layered Ocean Model, which is a descendent of the primitive equation model by Hurlburt and Thompson (1980) and which has been significantly enhanced by Wallcraft (1991). The model grid covers the globe from 72° S to 71° N. Results from model simulations using two different horizontal resolutions are discussed; they are the 0.5° (1/2°) model (0.5° lat. by 0.7° long.) and the 0.25° (1/4°) model (0.25° lat. by 0.35° long.) and are the resolutions for each model variable. Sensitivities to vertical resolution are also presented. The models have either one or three active upper layers, but the lowest layer is infinitely deep and at rest. These are commonly referred to as 1.5- and 3.5-layer models because they contain two and four layers, respectively, but represent only one and three internal vertical modes for the ocean. The mean layer depth is at 250 m for the 1.5-layer model and 135 m, 335 m, and 550 m for the 3.5-layer models. Large deviations from these mean interface depths occur. The models contain realistic coastline geometry and include such deep marginal seas as the Bering Sea, the Sea of Okhotsk, the Sea of Japan, the South China Sea, the Sulu Sea, and the Indonesian archipelago. They have horizontal mixing in the form of Laplacian friction and vertical exchange of momentum, mass, and heat. The models are thermodynamic, and horizontal density gradients within each layer can be modified by advection, diffusion, entrainment, and relaxation to an annual mean density climatology based on Levitus (1982). Although the models are thermodynamic and can accept thermal forcing functions, thermal forcing was not used in these hindcasts. As a result, sea surface height (SSH) anomalies due to seasonal heating and cooling are not included.

## 2.1 Atmospheric Forcing

Winds are the only time-dependent forcing for the models, and no synoptic ocean data are assimilated. The models were spun-up from rest to statistical equilibrium using the Hellerman and Rosenstein (1983) monthly mean wind stress climatology. To drive the model on interannual time scales, 1000-mbar winds from the European Centre for Medium-Range Weather Forecasts (ECMWF) were used. The combination of global coverage and a relatively consistent long time series led us to choose the ECMWF winds over those from other operational atmospheric centers. Ly et al. (1992) compared normalized ECMWF 1000-mbar, 10-m, and surface stress products and found few differences in temporal variability. Furthermore, the large-scale spatial fields were similar between all three products. The velocity components at 12-h intervals were converted to wind stress using a constant drag coefficient of  $1.5 \times 10^{-3}$  and  $\rho_{\text{air}} = 1.2 \text{ kg/m}^3$ ; then monthly averages were formed. In forming the surface stresses from the 1000-mbar winds, no directional changes were made.

Global simulations forced solely by the ECMWF 1000-mbar winds yield a southern branch of the South Equatorial Current (SEC) and a South Equatorial Countercurrent (SECC), which are too strong in comparison with observations, and a North Equatorial Countercurrent (NECC), which is  $1^\circ$  to  $2^\circ$  northward of its observed position. We determined that a more realistic mean state could be obtained in the ocean model by using a hybrid wind set. The ECMWF mean over the 1981–1990 time frame was subtracted from its monthly means and replaced by the Hellerman-Rosenstein annual mean. This hybrid wind set (E/H) was used to extend the integration already spun-up to statistical equilibrium using the Hellerman-Rosenstein monthly winds. Thus, the annual mean solution would still be driven primarily by the Hellerman-Rosenstein data, but seasonal and interannual forcing would come from ECMWF. All model results discussed use the E/H wind forcing.

## 3.0 MODEL RESPONSE TO LARGE-SCALE FORCING

Because the  $0.5^\circ$  model is basically non-eddy resolving and the  $0.25^\circ$  model is only marginally eddy resolving, they do not reproduce realistic mesoscale variability observed in such major current systems as the Kuroshio Extension or the Gulf Stream. In addition, the reduced-gravity models lack the barotropic mode and realistic bottom topography, which can play an important role in the flow instabilities. These instabilities are the primary cause of the observed mesoscale (50 to 500 km) variability. However, the model is able to directly reproduce wind-forced anomalies on intraseasonal to interannual time scales. The primary objective of this report is to examine this capability. These wind-forced anomalies include El Niño–Southern Oscillation events, sea-level variability, the position of fronts and currents, and current transport variability. The oceanic response to atmospheric forcing is most rapid in the tropics and that is predominantly where these wind-forced anomalies are found.

The model's ability to respond to large-scale, wind-forced anomalies is illustrated in Fig. 1, a global comparison of SSH anomalies from the  $0.25^\circ$  3.5-layer model and data from the U.S. Navy's *Geodesy Satellite-Exact Repeat Mission* (Geosat-ERM). The model was sampled along the 17-d repeat tracks of the Geosat-ERM at the same times as the satellite. The Geosat-ERM data set was obtained from the National Oceanic and Atmospheric Administration (NOAA). The data set contained satellite orbit solutions based on the Goddard Earth Model T2 gravity field (Haines et al. 1990). Atmospheric corrections supplied by NOAA were applied to the data, and estimates of the major ocean and solid earth tides were removed from the data (Cheney et al. 1987). An estimate of the error in the orbit solutions was removed, as well as an estimate of the error in the M2 tide component (Jacobs et al. 1992). Both the model and Geosat-ERM data covered from 6 November 1986 to 31 December 1990. The mean SSH over time was computed at each point along the ground track and subtracted from the data, thus producing SSH anomalies. Data were

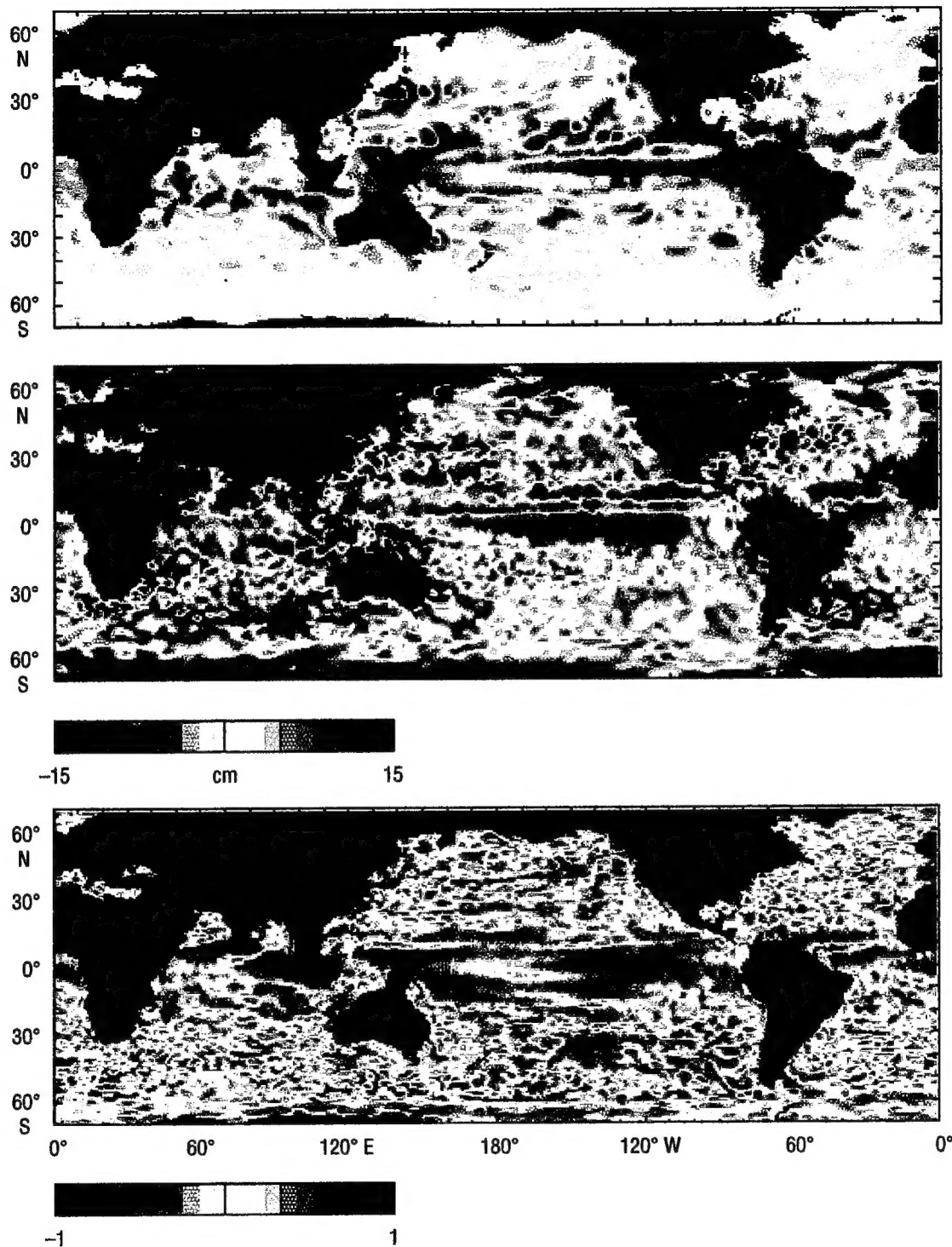


Fig. 1 — A comparison of SSH anomalies in the  $0.25^{\circ}$  3.5-layer model and the Geosat-ERM. (a) Model SSH deviation for repeat cycle 41 (20 September–7 October 1988). (b) Geosat-ERM SSH deviation for the same repeat cycle. Both deviation plots are with respect to the mean SSH for the first 43 repeat cycles (8 November 1986–10 November 1988). The color bar is in centimeters. (c) The correlation between the model and the Geosat SSH anomalies over the first 43 repeat cycles. The color bar ranges between  $\pm 1$ .

mapped to a  $0.5^\circ \times 0.5^\circ$  grid by a weighted averaging scheme where the weighting was given by a Gaussian function with a 200-km length scale (Zlotnicki et al. 1989).

The upper panel in Fig. 1 shows the model SSH deviation for repeat cycle 41 (20 September–7 October 1988), and the middle panel is the SSH deviation from Geosat-ERM for the same repeat cycle. Some striking similarities can be seen between the two anomaly fields. These similarities include a distinctive narrow band of positive anomaly across most of the Pacific Ocean between  $5^\circ$  and  $10^\circ$  N. Negative anomalies appear on either side of it in the central and eastern basin. In the Geosat-ERM data, one might think this band of positive anomaly is the result of water vapor error associated with the intertropical convergence zone, but the anomaly also appears in the model, which is not subject to that type of error. Both also show relatively high sea level in the western equatorial Pacific Ocean, and the tilt of the SSH along the equator is similar. Additionally, a positive anomaly in both data sets is seen to extend into the equatorial Indian Ocean off the west coast of Australia. Similarities can also be seen in the equatorial Atlantic.

Similarities between the model SSH deviations and those from Geosat-ERM can be seen in other regions, but areas of disagreement also exist. The best agreement is at the low latitudes where there is a relatively rapid response to changes in the wind fields. This is shown in the lower panel of Fig. 1, the correlation in SSH anomaly between the model and Geosat-ERM over the first 43 repeat cycles. Note the bands of high positive correlation across the equatorial latitudes. At mid to high latitudes, mesoscale flow instabilities and seasonal anomalies due to heating and cooling also contribute to the SSH variability. However,  $0.25^\circ$  resolution cannot adequately resolve the flow instabilities, and the model lacks the steric anomalies; thus, correlations at these latitudes are low. They are also low in the subpolar latitudes due to model interface ventilation (discussed below).

A similar model/Geosat-ERM SSH anomaly comparison can be found in Hurlburt et al. (1992) for the  $0.5^\circ$  1.5-layer global model and in Metzger et al. (1992) for the  $0.5^\circ$  3.5-layer global model. The results for the  $0.5^\circ$  1.5- and for the  $0.5^\circ$  and  $0.25^\circ$  3.5-layer models are similar. However, a significant difference is found in the eastern equatorial Pacific where the negative (blue) SSH anomaly along the equator is strongest farther to the west in the 3.5-layer models, as observed in the Geosat-ERM data. This expansion of negative SSH anomaly is due to vertical mixing in the 3.5-layer models associated with the equatorial undercurrent in the eastern Pacific. With only one active layer, the 1.5-layer model cannot have an undercurrent.

These results show that the model is able to hindcast observed wind-forced oceanic anomalies, a positive note for the atmospheric forcing from ECMWF, as well as for the ocean model. Given accurate atmospheric forcing, the model should exhibit intraseasonal to interannual variations similar to those seen in in situ data. After a brief discussion of the model climatology, the remainder of this report focuses on the tropical latitudes based on the preceding results. Comparisons will be made among the model, the drifting buoys, and the island/coastal sea-level stations.

#### 4.0 MODEL CLIMATOLOGY

The discussion of the model climatology concentrates on the circulation in the Pacific Ocean north of  $20^\circ$  S, since the remaining model/data comparisons are in this basin. Figure 2 shows the 1981–1990 mean SSH field overlaid with currents for the  $0.25^\circ$  3.5-layer model. With a few exceptions, the mean solution is similar for all the models discussed here.

The large cyclonic subpolar and anticyclonic subtropical gyres are separated by the Subarctic Front at  $42^\circ$  to  $47^\circ$  N. At subpolar latitudes, the model produces a relatively flat SSH field within

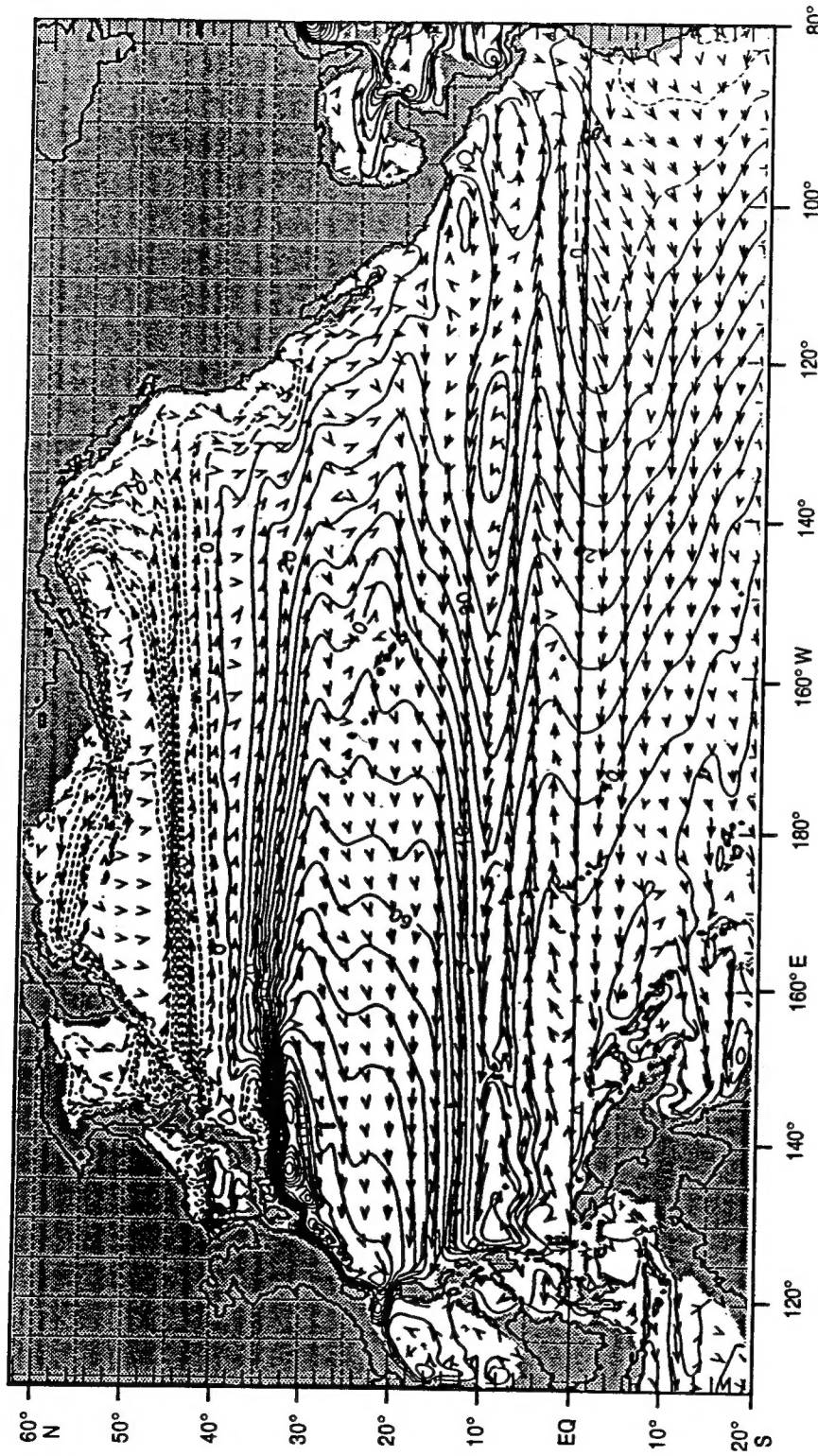


Fig. 2 — The 1981–1990 mean SSH field overlaid with currents from the  $0.25^\circ$  3.5-layer global model. Only a subregion is shown, the Pacific Ocean north of  $20^\circ$  S. The contour interval is 5 cm. Shaded areas represent model land, i.e., regions shallower than 200 m (with a few exceptions).

the interior of the subpolar gyre. The flatness is a result of positive wind stress curl, which raises the interfaces between the layers. To prevent the interfaces from surfacing, vertical mixing is used. Most of the wind energy in these regions with flat SSH is lost to the infinitely deep abyssal layer, and the active layers are shallow and flat. Thus, the model has no significant geostrophically balanced currents or anomalies in the interior of the subpolar gyres.

The strongest portion of the subtropical gyre is bounded on the north by the Kuroshio Extension at  $32^{\circ}$  to  $36^{\circ}$  N, giving a double frontal structure that separates the two gyres. The southern half of the subtropical gyre consists of broad, westward return flow that intensifies to the west and the south as the North Equatorial Current (NEC) at  $10^{\circ}$  to  $18^{\circ}$  N. At  $153^{\circ}$  W, the strength of the NEC in the model is weaker than the observations of Wyrtki and Kilonsky (1984). Their data from the Hawaii-to-Tahiti Shuttle Experiment indicate an NEC transport of  $23.3$  Sv ( $1$  Sv =  $10^6$  m $^3$ s $^{-1}$ ) to the west in approximately the upper 300 m. The transport in the upper two layers of the  $0.25^{\circ}$  model is  $15.9$  Sv. Differences between observational versus model transports could be due to interannual variability. The model transports were computed over a 10-yr time series, whereas the Wyrtki-Kilonsky observations span from January 1979 to June 1980. Furthermore, variations in the latitudinal extent of the NEC in relation to where the model was sampled could cause the differences.

Near the Philippine coast at approximately  $14^{\circ}$  N, the NEC splits into the northward-flowing Kuroshio Current and the southward Mindanao Current. This split point varies by about a degree among the various models, but all are in close agreement with the observed dynamic height from the Navy's Generalized Digital Environmental Model (GDEM) climatology (Teague and Hogan 1989; Hurlburt et al. 1989); GDEM places the split point near  $14.5^{\circ}$  N. Observational transport estimates of the Mindanao Current ranged from  $8$  to  $40$  Sv, and Lukas et al. (1991) present a good summary table. However, comparison can be difficult because of the various methods that define both the vertical and horizontal extent of the Mindanao Current. Along  $8^{\circ}$  N, from the Philippine coast out to  $129.5^{\circ}$  E, the upper three layers of the  $0.25^{\circ}$  model exhibit a mean southward transport of  $28.6$  Sv for the Mindanao Current. This number is well within historical estimates and is close to the quasi-synoptic geostrophic estimate of  $26$  Sv across  $8^{\circ}$  N by Lukas et al. (1991).

In the model the Mindanao Current flows around the Mindanao Eddy, centered at  $5^{\circ}$  N,  $127^{\circ}$  E, and merges with the SEC to form the eastward-flowing NECC, which is centered near  $5^{\circ}$  N and extends across the width of the basin. At  $153^{\circ}$  W, the  $0.25^{\circ}$  model has eastward flow in all three layers, but the strongest flow is trapped in the upper layer. The Wyrtki-Kilonsky observations separate the upper and lower layer flows near 170 m. This lower layer flow is the Northern Subsurface Countercurrent (NSCC), which corresponds to layers two and three in the model. Although the absolute magnitude of the model transports is approximately 30% weaker than the observations, the ratio of the NSCC to the NECC (40%) agrees well. The model shows the SECC at  $7^{\circ}$  to  $10^{\circ}$  S, but it is much weaker than the NECC and is confined to west of the dateline.

The  $0.25^{\circ}$  model transport value of the Equatorial Undercurrent (EUC) is  $25.4$  Sv at  $153^{\circ}$  W. This number is slightly lower than the observational estimates of  $32.3$  Sv by Lukas and Firing (1984) and  $30.5$  Sv by Wyrtki and Kilonsky (1984) at this same longitude. However, the  $0.5^{\circ}$  3.5-layer model EUC transport value of  $29.2$  Sv agrees better. Recent research (not shown) in determining the layer structure and improving the vertical mixing scheme has brought the  $0.25^{\circ}$  results in closer agreement with the observations.

The model also accurately depicts the SSH tilt across the Pacific basin at the equator. Philander (1990) indicates that the observed west-to-east decrease is approximately 50 cm, the same as the model.

A detailed description of the model climatology in the other ocean basins will not be presented here, but the model can represent the basic upper ocean features in these domains. In the Indian Ocean, the reversals of the Arabian Sea and Bay of Bengal current systems that result from the seasonal monsoonal circulation are depicted; however, the complex eddy structure off the coast of Somalia during the southwest monsoon is not clearly seen in the  $0.5^\circ$  model. These eddies are better defined in the  $0.25^\circ$  model. The large-scale circulation in the Atlantic Ocean is simulated, although the representation of the Gulf Stream is unrealistic. In part, this unrealism can be attributed to the lack of a realistic thermohaline circulation and associated deep western boundary currents, which play an important role in this basin (Gordon 1986; Schmitz and Richardson 1991). More recent simulations with an oxygen-based detrainment scheme have a more realistic thermohaline circulation and show the global “conveyor belt” circulation (Gordon 1986). In the tropical Atlantic, the models discussed here depict the retroflection of the Brazil Current near  $6^\circ$  to  $8^\circ$  N, but simulate little or no Atlantic EUC, again a situation remedied in more recent simulations.

## 5.0 WIND FORCING VERSUS FLOW INSTABILITIES IN OCEANIC ANOMALY GENERATION

The root-mean-square (rms) SSH field for the Pacific Ocean is seen in Fig. 3a. This field was computed over the 1985–1990 time frame and is the SSH variability over two  $0.25^\circ$  3.5-layer model simulations driven by E/H wind forcing (see discussion below). The only difference between these simulations is the initial state; the second realization was started from the end of the first. Note the area of large SSH variability to the south and east of Japan associated with the meandering and eddy shedding of the Kuroshio Current. The rms SSH reaches a maximum of 55 cm in this region. A relative maximum is also evident along  $15^\circ$  N, the latitude of the NEC. Interannual variations in both the strength and position of the NEC contribute to these SSH variations. Hurlburt et al. (1992) noted similar results from a  $0.125^\circ$  ( $1/8^\circ$ ) 6-layer model of the Pacific. Two regions of relatively high variability are shown east of the Philippines in the western equatorial Pacific. The northern region is enhanced variability of the NEC as it approaches the Philippine coast and is due to variations in the location of the NEC split point. The southern region is due to meandering of the NECC along  $5^\circ$  N.

Because the two  $0.25^\circ$  model simulations were identical except for the initial state, the differences between them should be due to mesoscale flow instabilities. A technique was developed to separate the total SSH variability field into two components, one caused by direct atmospheric forcing (deterministic) and the other due to mesoscale flow instabilities (not deterministic). Spatial maps were then created to determine the relative importance of the two anomaly generation mechanisms. To calculate the maps, first the mean SSH over 1985–1990 was computed for each  $0.25^\circ$  model realization and then subtracted from each record (3.05 d apart) of the corresponding simulation to form SSH anomaly fields ( $\eta$ ). At each gridpoint, the temporally corresponding records of the two realizations were then combined and averaged as follows:

$$\overline{\eta^2} = \bar{\eta}^2 + \overline{\eta'^2}. \quad (1)$$

Each component (term in (1)) was then temporally averaged over 1985–1990. The left side represents the total SSH variability (Fig. 3a), and the right side represents the SSH variability due to atmospheric forcing plus the SSH variability due to flow instabilities. However, because there are only two realizations, the separation of these two contributions to the temporal SSH variability is not complete. The flow instabilities component is underestimated and the wind-forced component is overestimated. This is especially true in the Kuroshio Extension region as two realizations are not

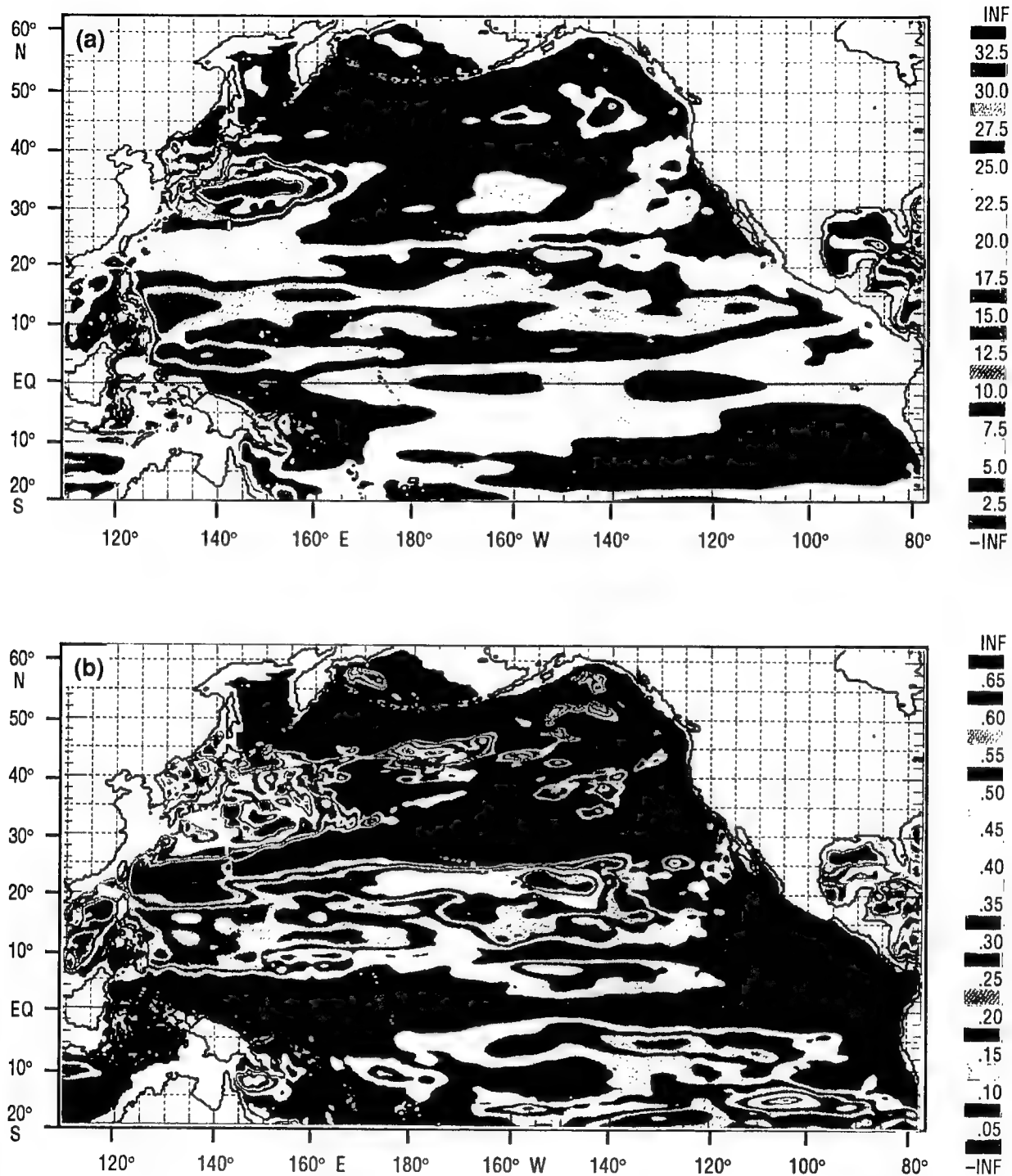


Fig. 3 — (a) The rms SSH from two realizations of the  $0.25^\circ$  3.5-layer global model. Only a subregion is shown, the Pacific Ocean north of  $20^\circ$  S; contour interval is 2.5 cm. (b) Percent of the SSH variability associated with flow instability effects. This field has been normalized by the total SSH variability. Blue and purple areas indicate where wind forcing dominates; orange and red areas indicate regions where flow instability mechanisms are important; contour interval is 5%.

sufficient to average all flow instability effects. Nonetheless, these fields at least indicate regions where the two instability mechanisms are important. The maps from this technique would also be more realistic if applied to a model that is fully eddy resolving and that contains the barotropic mode and realistic bottom topography—features important to the realistic simulation of the flow instabilities.

By dividing Eq. (1) by the term on the left side, we can obtain maps of the fraction of the SSH variability due to atmospheric forcing or flow instabilities.

$$1 = \frac{\overline{\eta}^{-2}}{\overline{\eta}^2} + \frac{\overline{\eta'}^2}{\overline{\eta}^2}. \quad (2)$$

Figure 3b is a map of the fraction due to flow instabilities. From Eq. (2), the areas of purple and blue are regions where SSH variations are controlled largely by the wind forcing, whereas mesoscale flow instabilities are more important in the orange and red areas. The region off the coast of Japan is dominated by SSH variability due to flow instabilities, but pockets of local minima exist due to an overestimation of the wind-forced component. Other regions where flow instabilities are relatively important are a band that spans the Hawaiian Islands, the Sea of Japan, a band along the Subarctic Front, and the area east of the Philippines. A band of small values along the equator indicates that SSH variability is due almost entirely to wind forcing. In this region, accurate atmospheric forcing can give a relatively accurate hindcast of the SSH variability.

## 6.0 UPPER-OCEAN TRAJECTORY FIELDS

The next model/data comparison focuses on the western equatorial Pacific Ocean where the upper layer current field from the model is compared to that determined from trajectories of drifting buoys drogued at 10 m and acoustic Doppler current profiler (ADCP) data. The observational data were obtained during the Western Equatorial Pacific Ocean Circulation Study III (WEPOCS III) and were analyzed by Lukas et al. (1991); they provide an excellent quasi-synoptic view of the upper ocean. Figure 4a shows the mean July–September 1988 velocity vectors averaged on  $1^\circ$  squares. A 9-point smoother was applied to the data. It includes both drifting buoy and ADCP data and has been plotted on the model topography for ease of comparison. The upper layer currents from the models averaged over the same period are as follows: Fig. 4b is the  $0.5^\circ$  1.5-layer model, Fig. 4c is the  $0.5^\circ$  3.5-layer model, and Fig. 4d is the  $0.25^\circ$  3.5-layer model.

Figures 4d and f are an average of two  $0.25^\circ$  3.5-layer model simulations. With increased horizontal resolution and a much lower eddy viscosity ( $300 \text{ m}^2 \text{ s}^{-1}$  vs.  $1500 \text{ m}^2 \text{ s}^{-1}$  for the  $0.5^\circ$  3.5-layer model and  $2000 \text{ m}^2 \text{ s}^{-1}$  for the  $0.5^\circ$  1.5-layer model), flow instabilities are more pronounced in the  $0.25^\circ$  model compared to the  $0.5^\circ$  models. Thus, given the same atmospheric forcing, a small perturbation in the initial state could cause the two hindcasts to differ significantly. To lessen these flow instability effects as seen in Fig. 3b, an average of the two  $0.25^\circ$  model simulations is used.

The agreement between the WEPOCS III data and the three model simulations is generally good. All show the southward-flowing Mindanao Current along the east coast of the Philippines and its bifurcation in the Sulawesi (formerly Celebes) Sea. The WEPOCS III data indicate the westward branch is strongest in the northern Sulawesi Sea with some eastward recirculation in the south. The  $0.25^\circ$  model (Fig. 4d) agrees well in the region. There is some disagreement between the  $0.5^\circ$  models (Fig. 4b and c) and the observed data concerning this westward branch. The  $0.5^\circ$  models show

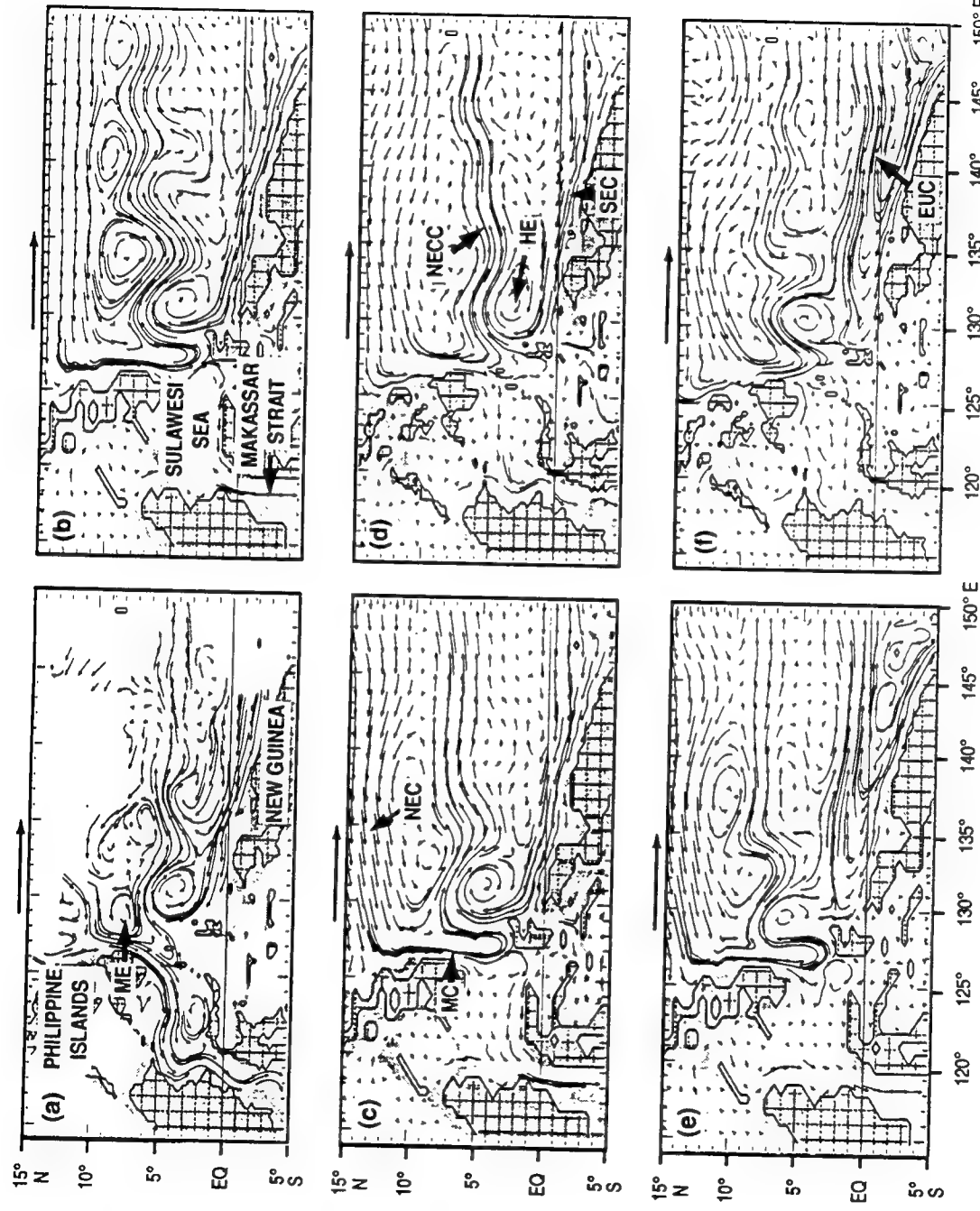


Fig. 4—(a) Mean July–September 1988 velocity vectors averaged over  $1^{\circ}$  squares; includes both drifting buoy and ADCP data (adapted from Lukas et al. (1991)). Upper layer currents averaged over the same period for (b) the  $0.5^{\circ}$  1.5-layer model, (c) the  $0.5^{\circ}$  3.5-layer model, and (d) the average of two  $0.25^{\circ}$  3.5-layer model simulations. Layer two currents averaged over the same period for (e) the  $0.5^{\circ}$  3.5-layer model and (f) the average of two  $0.25^{\circ}$  3.5-layer model simulations. The reference vector above (a)–(d) is  $1.0 \text{ m/s}^{-1}$  and  $0.5 \text{ m/s}^{-1}$  for (e) and (f). ME – Mindanao Eddy, MC – Mindanao Current, and HE – Halmahera Eddy.

westward flow across the entire Sulawesi Sea, which strengthens to the south. Despite this disagreement, all three models and the observed data indicate that the Mindanao Current is the primary water mass source for Pacific to Indian Ocean throughflow via the Makassar Strait. This determination agrees with the global simulations described in Kindle et al. (1989) as well.

The remaining branch of the Mindanao Current flows southward a short distance, turns eastward around the Mindanao Eddy ( $8^{\circ}$  N,  $129^{\circ}$  E in the observations and the  $0.25^{\circ}$  model), and feeds the NECC. All the models depict this phenomenon—some with more success than others. South of Mindanao, the two  $0.5^{\circ}$  models (Fig. 4b and c) have stronger southward flow than is observed and the center of the Mindanao Eddy is too far south. The  $0.25^{\circ}$  model (Fig. 4d) agrees best with the WEPOCS III data south of Mindanao, possibly because the  $0.25^{\circ}$  model is better able to resolve the complex geometry of this region. Note that both Sangihe and Talaud Islands are seen near  $3^{\circ}$ – $4^{\circ}$  N,  $126^{\circ}$ – $127^{\circ}$  E. The surface flow between these two islands agrees with observations reported by Wyrtki (1961).

The SEC crosses the equator along the north coast of New Guinea and is relatively strong in both the models and the observed data. Near  $2^{\circ}$  N,  $134.5^{\circ}$  E, the WEPOCS III data indicate a small northward branch emanating from the SEC, which feeds the NECC. Both  $0.5^{\circ}$  models bifurcate at this longitude, but the  $0.25^{\circ}$  model does not. The main branch of the SEC joins the Mindanao Current near  $3^{\circ}$  N,  $128^{\circ}$  E to help feed the NECC. North of the SEC two anticyclonic eddies appear in the observed data. The one centered near  $4^{\circ}$  N,  $131^{\circ}$  E is the Halmahera Eddy. The location and shape of the Halmahera Eddy is better represented in the two  $0.5^{\circ}$  model simulations. The  $0.25^{\circ}$  model places the eddy slightly too far south and its shape is somewhat elongated. The anticyclonic eddy to the east of the Halmahera Eddy is seen in all model simulations, but the position and the shape vary from the observations.

The observed data show the NECC centered along  $5^{\circ}$  N. At  $133^{\circ}$  E, a large meander exists with a smaller, less distinct meander at  $139^{\circ}$  E. All three models agree well with the longitudinal location of the first meander, although the amplitude varies among them. The amplitude of this meander is quite large in the  $0.5^{\circ}$  1.5-layer model. With only one active layer, all the wind-driven energy is trapped in one layer and stronger currents exist. In contrast, the  $0.5^{\circ}$  3.5-layer model has a smaller meander. With an increase in the number of layers, barotropic instability is decreased in this region and the energy is spread out more among the layers; weaker upper layer currents exist.

Figures 4e and f show the second layer currents for the  $0.5^{\circ}$  3.5-layer and  $0.25^{\circ}$  3.5-layer models, respectively. These figures show the dramatic change in the current structure between the upper two layers. In the second layer the eastward branch of the Mindanao Current flows around the Halmahera Eddy and feeds a weaker NECC. It also joins with the SEC along the north coast of New Guinea and feeds the eastward EUC. Finally, the  $0.25^{\circ}$  3.5-layer model (Fig. 4f) shows a westward current near  $3^{\circ}$ – $5^{\circ}$  N,  $138^{\circ}$ – $150^{\circ}$  E, which is not present in the upper layer. It branches to feed both the NECC and the EUC.

In an effort to quantify this analysis, vector correlations were computed between the WEPOCS III data, and the model results after the model data were linearly interpolated to the  $1^{\circ}$  observational grid. On the order of 250 points were used to compute the correlations. In the observations, the NECC is the dominant, strongly time-varying feature. Thus, the correlations are strongly affected by the model's positioning of this current. Those simulations that do well in positioning the NECC and the Halmahera Eddy have higher correlations.

Table 1 shows the vector correlations between the smoothed July-August-September (JAS) 1988 drifting buoy/ADCP data and the various model JAS means for all the years of the simulations

Table 1 — Vector correlations among JAS 1988 WEPOCS III drifting buoy/ADCP data from Lukas et al. (1991) and the various model JAS means (columns 2–4). A nine-point smoother was applied to the WEPOCS III data. Correlations between the JAS 1988 model mean from one  $0.25^\circ$  realization versus the various JAS model means from the second  $0.25^\circ$  realization (column 5). Correlations among an average of two  $0.25^\circ$  3.5-layer models and two Richardson-McKee and Levitus ship drift climatologies (columns 6–7). Model-model and model-climatology correlations were limited to those points where observational WEPOCS III data existed.

Year	Models vs. WEPOCS III JAS 1988 Observations			Model vs. Model	0.25° 3.5-Layer Model vs. Ship Drift Climatology	
	0.5° 1.5-Layer	0.5° 3.5-Layer	0.25° 3.5-Layer		0.25° 3.5-Layer	Richardson- McKee
1990	—	—	0.46	0.54	0.54	0.55
1989	0.54	0.65	0.62	0.60	0.63	0.63
1988	0.61	0.62	0.68	0.82	0.69	0.66
1987	0.52	0.53	0.51	0.45	0.71	0.60
1986	0.49	0.49	0.52	0.43	0.64	0.56
1985	0.57	0.57	0.48	0.47	0.56	0.53
1984	0.20	0.17	0.13	-0.01	0.20	0.12
1983	0.18	0.15	0.02	0.08	0.05	0.01
1982	0.52	0.51	0.28	0.30	0.35	0.33

(columns 2–4). (These results can be compared to Table 1 of Metzger et al. (1992), which used unsmoothed WEPOCS III data.) Again the  $0.25^\circ$  3.5-layer model results are for the average of two realizations. Except for one case, the JAS 1988 WEPOCS III data correlate better with the model JAS 1988 mean data than with the model JAS mean for any other year. This result also applies to both individual realizations of the  $0.25^\circ$  model (not shown). The  $0.25^\circ$  model results for 1988 are better than either of the  $0.5^\circ$  models, and it also discriminates the agreement with 1988 from the other years the best. The one exception is the  $0.5^\circ$  3.5-layer model, which produces a slightly higher correlation for the 1989 JAS model mean than for 1988; in this model the position of the NECC in 1989 is closer to the observations than the hindcast for 1988. The large year-to-year changes in the correlation with the 1988 observations demonstrate significant interannual variability in the position and strength of the NECC and the Halmahera Eddy. It should be noted, however, that part of the interannual variability appears to result from operational changes in the ECMWF atmospheric forcing products.

Listed in column five of Table 1 are vector correlations of the JAS 1988 model mean from one realization of the  $0.25^\circ$  model versus the JAS model mean for the various years from the second realization. The model-model correlation calculations were limited to the points where observational data existed. Differences between these two  $0.25^\circ$  simulations are attributed mainly to flow instabilities. The verification year has the highest correlation (0.82), but the off-year correlations to 1988 are very similar to the off-year observation versus model correlations (columns 2–4) and they exhibit the same degree of interannual variability. The correlations are only slightly improved in the off-years when comparing the JAS mean from one realization with the JAS

1988 mean from the same realization (not shown). Although the effect is small, this suggests long-term anomalies due to flow instabilities and/or long-term memory due to differences in the initial state that might influence this region. The Pacific to Indian Ocean throughflow via Indonesia is a likely contributor to this long-term memory. Although the throughflow exhibits strong seasonal variability, the annual mean throughflow is relatively slow to equilibrate due to the global origins of this feature. Also computed but not shown were year-by-year correlations between the two  $0.25^\circ$  realizations. The 1988 value of 0.82 shown in column 5 is the median correlation for 1982 through 1990, which ranged from 0.73 to 0.94.

The detailed agreement among the observations and the three models is somewhat surprising, not only because of the complexity of the region but also because all of the models show the western equatorial Pacific as a region that exhibits relatively strong flow instabilities as discussed above. These have characteristic time scales of 1 to 4 months. Therefore, 3 months is a short time to average them out. In addition to flow instabilities and shortcomings in the models, gross differences in sampling and errors in the atmospheric forcing are other major reasons for differences between the models and the observations.

Vector correlations between the WEPOCS III data and the climatological ship drift data sets by Richardson and McKee (1989) and Levitus (unpublished) are shown in Table 2. The ship drift data are JAS means, and a nine-point smoother was applied to the Richardson-McKee climatology in column 4; no smoothing was performed on the Levitus climatology. Note that the smoothed Richardson-McKee and Levitus climatologies correlate at 0.85 when limited to the WEPOCS III data locations. This result is essentially unchanged (0.83) if the two climatologies are correlated using all common data points within the western equatorial Pacific region shown in Fig. 4.

In a climatological sense, how "normal" are the JAS 1988 WEPOCS III data? Lukas et al. (1991) qualitatively compared their observations with climatological ship drift data and suggest their measurements were typical for the region. Our quantitative analysis supports this judgment. The WEPOCS III data have a 0.72 vector correlation with both ship drift climatologies.

The models further suggest that 1988 was near its climatological state. In Table 1, columns 6–7, vector correlations between the JAS ship drift climatologies and the  $0.25^\circ$  model JAS means for all the years of the simulation are shown. The same degree of interannual variability exists in the correlations between the  $0.25^\circ$  model and the ship drift climatologies as in the correlations

**Table 2 — Vector correlation among JAS climatological Levitus ship drift data, JAS climatological Richardson-McKee ship drift data, smoothed (9 pt) JAS climatological Richardson-McKee ship drift data, JAS 1988 WEPOCS III drifting buoy/ADCP data from Lukas et al. (1991). Correlations were limited to the WEPOCS III data locations.**

	Levitus	Richardson-McKee	Richardson-McKee (Smoothed)	WEPOCS III (Unsmoothed)	WEPOCS III (Smoothed)
Levitus	1.00	0.64	0.85	0.61	0.72
Richardson-McKee	—	1.00	0.86	0.56	0.58
Richardson-McKee (smoothed)	—	—	1.00	0.65	0.72
WEPOCS III	—	—	—	1.00	0.94
WEPOCS III (smoothed)	—	—	—	—	1.00

between the models and the WEPOCS III data. Here, 1988 had the highest correlation with the Levitus data and the second highest correlation with Richardson-McKee data. Results from the 0.5° models (not shown) are similar, but the distinction of 1988 correlating highest with the ship drift climatologies is not as apparent. In general, though, 1988 did have some of the higher correlations.

Finally, it is encouraging to note the 0.25° model in 1988 has a correlation with the WEPOCS III data that is similar to the ship drift climatologies. This correlation suggests that when nonclimatological conditions exist, the models should provide estimates of the near-surface current fields that are superior to those from ship drift climatologies.

## 7.0 ISLAND/COASTAL SEA-LEVEL COMPARISON

The Integrated Global Ocean Services System (IGOSS) Sea Level Program makes island and coastal data available in the form of monthly means. The time series represents deviations from the 1975–1986 mean sea level computed for each station; all data have been quality controlled and any large linear trends have been removed. Sea-level time series from the model were extracted at the gridpoints closest to the island/coastal station. Since the model land/sea boundary is the 200-m isobath, the sampling points may differ by up to a few degrees—a point to consider in comparing the results. The long-term mean has also been subtracted from the model sea-level time series.

Comparisons between the three global models and the observed IGOSS monthly sea-level data were conducted for 29 island and coastal stations in the Pacific Ocean. The majority of stations are in the tropical latitudes, but a few are located at midlatitudes, e.g., Neah Bay, WA, and Crescent City, CA. Figure 5 shows the location of the IGOSS stations plotted on the model domain. The comparison for Tumaco, Colombia, a coastal station in the eastern Pacific located near 2° N, 79° W, is shown in Fig. 6. The upper panel (Fig. 6a) shows the IGOSS data plotted with the

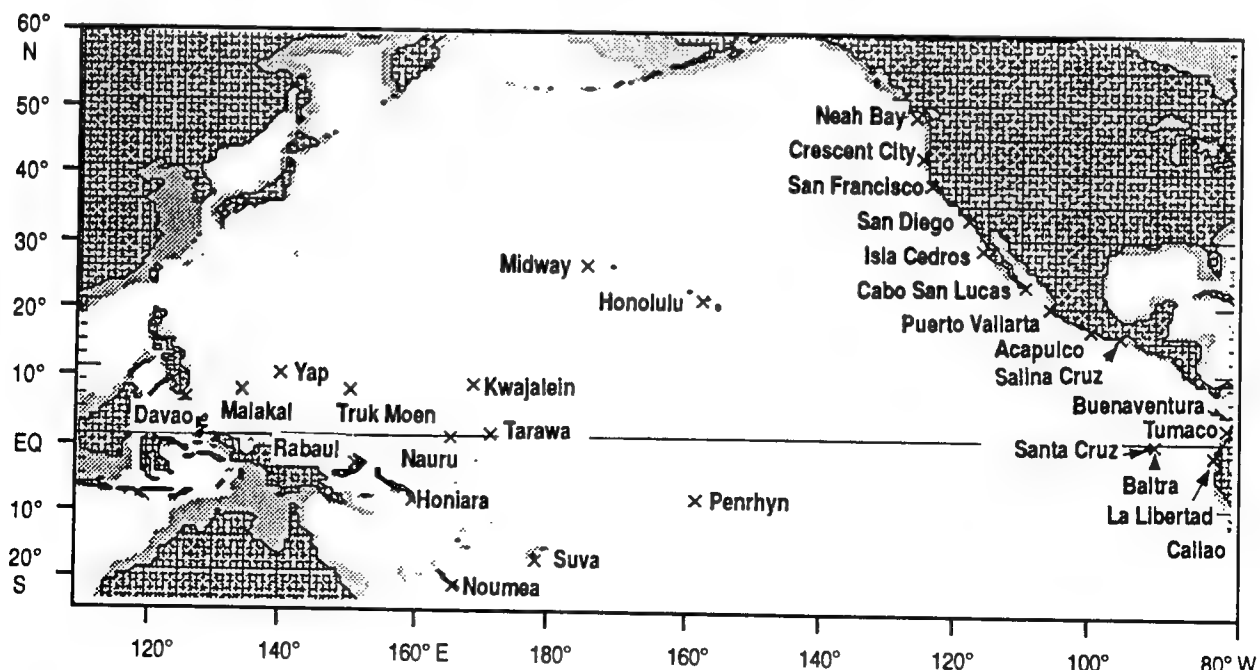


Fig. 5 — Locations of the IGOSS Sea Level Program island/coastal stations plotted on the model domain

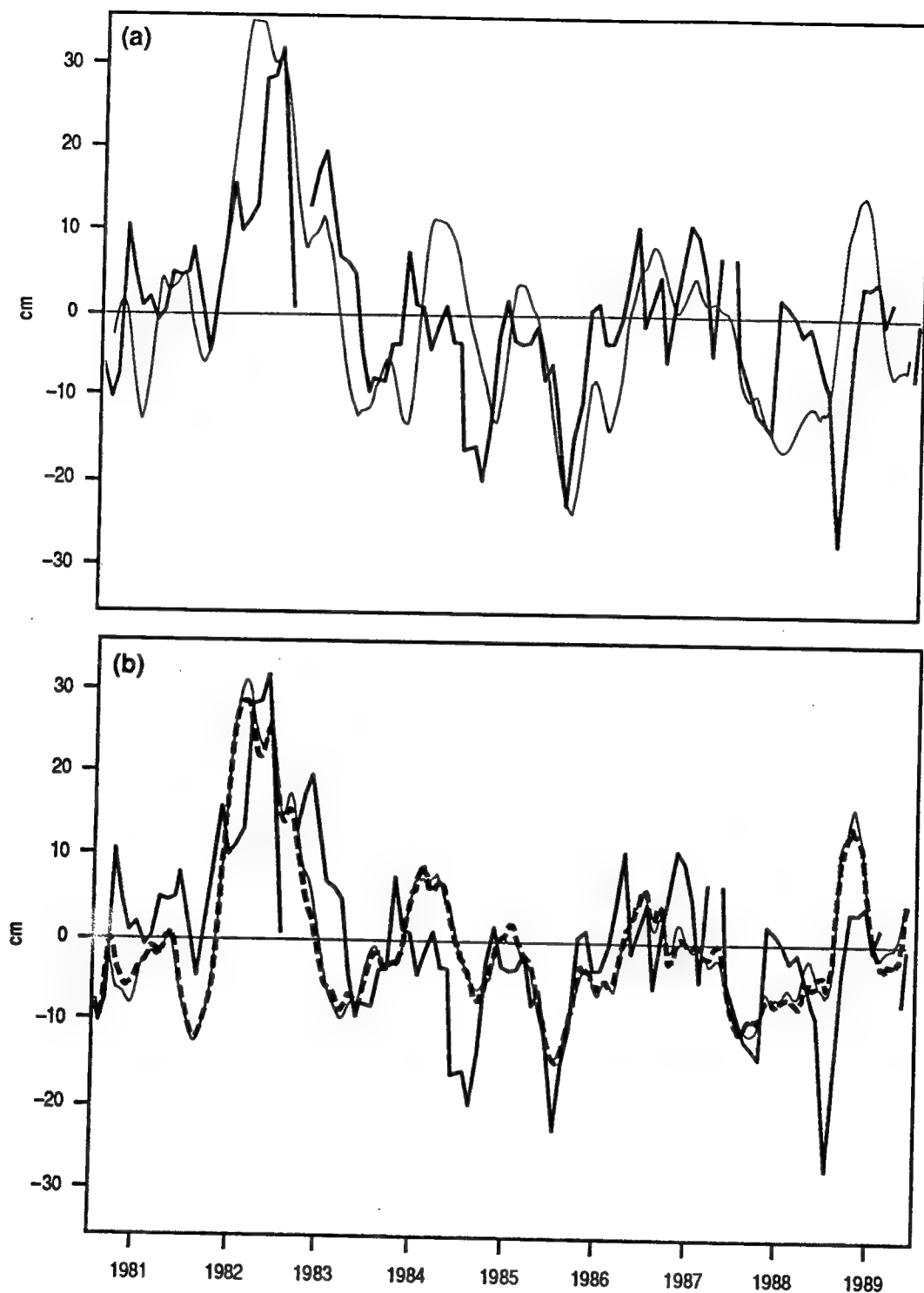


Fig. 6 — Monthly sea-level data for Tumaco, Colombia ( $1^{\circ}50' \text{ N}$ ,  $78^{\circ}44' \text{ W}$ ); a 30-day running mean has been applied to the model data. (a) Observed IGOSS data (heavy line) and the  $0.5^{\circ}$  1.5-layer model (thin line). (b) Observed IGOSS data (heavy line),  $0.5^{\circ}$  3.5-layer model (thin line), and the  $0.25^{\circ}$  3.5-layer model (dashed line).

$0.5^\circ$  1.5-layer model; the lower panel (Fig. 6b) shows the IGOSS data plotted with the  $0.5^\circ$  and  $0.25^\circ$  3.5-layer models. In this region, all three models produce a similar time series. In general, the models are able to reproduce the interannual sea-level variations quite well. This ability is especially true in the example shown; the large increase in sea level associated with the 1982–1983 El Niño is clearly seen in all data sets. This comparison provides a measure of confidence in the atmospheric forcing data and in the ability of the model to respond to the forcing on these time scales.

On seasonal and intraseasonal time scales the models have mixed success. At times they are able to reproduce both the phase and the amplitude of the sea-level signal, but frequently both are in error. Generally, the variability about the mean is also weaker in the models than in the IGOSS data. This is probably partly due to the use of monthly mean wind forcing. Since the Nyquist frequency is 2 months, perhaps the best to be expected is for the models to resolve the semiannual time scale. However, recent work (Kindle and Phoebus 1993) has indicated that the model can respond at much higher frequencies. After forcing the model with daily averaged winds, SSH correlations between the model and Baltra, Ecuador, were as high as 0.78 with small differences in phase.

To quantify this comparison, correlation coefficients between the IGOSS and model data have been computed (Table 3); the values for the  $0.25^\circ$  model are again averages for the two realizations. If there were two realizations from the  $0.5^\circ$  model and the results were also averaged, it is expected that the correlations would be slightly higher. However, the flow instability effects would not be nearly as pronounced as they are in the  $0.25^\circ$  simulations. The correlations are generally good; however, there are a few cases where the model does not accurately determine the sea level (Noumea and Midway). In the eastern tropical Pacific, the  $0.5^\circ$  1.5-layer model represents observed sea-level variability with accuracy equivalent to its 3.5-layer counterparts; exceptions to this are a few stations along the coast of Mexico. But, the addition of multiple layers (compare columns  $0.5^\circ$  1.5-layer and  $0.5^\circ$  3.5-layer) leads to an overall improvement in the statistics. Most notable are Nauru and Tarawa, which are located near the equator in the Gilbert Islands.

As shown in Fig. 4, a major equatorial current system is added to the model when the vertical resolution is increased from 1.5 to 3.5 layers. In the second layer, these currents are the eastward EUC and the westward currents that parallel the system to the north and south (Fig. 4f). The 3.5-layer models also produce a more realistic SEC than the 1.5-layer model. In the former, the SEC extends a few degrees into the Northern Hemisphere; in the latter, a broad NECC unrealistically spreads into the Southern Hemisphere. Associated with improvements in the 3.5-layer models is an improved circulation in the Solomon Sea and a higher correlation at Rabaul.

An increase in horizontal resolution (compare columns  $0.5^\circ$  3.5-layer and  $0.25^\circ$  3.5-layer) does not significantly improve the correlations. Overall, the statistics from the  $0.25^\circ$  3.5-layer model are equivalent to or slightly improved compared to the  $0.5^\circ$  3.5-layer model. The higher resolution permits a greater fraction of the variability to occur in the form of flow instabilities that are not a direct response to atmospheric forcing. In some cases this variability leads to substantial decreases in correlation; the most serious degradation can be seen at Honolulu. (Note in Fig. 3b the large area around the Hawaiian Islands where anomalies due to flow instabilities are larger than those due to atmospheric forcing.) These flow instabilities are a result of large anticyclonic eddies that propagate past Hawaii in the return flow of the subtropical gyre. These eddies have unrealistically large sea-level amplitude in this model, but are not well resolved at  $0.5^\circ$ , nor are they found at such large amplitude in the  $0.125^\circ$  6-layer Pacific model with realistic bottom topography discussed by Hurlburt et al. (1992).

Table 3 — Correlation coefficients among observed Integrated Global Ocean Services System (IGOSS) sea-level data and the global models. The IGOSS data are monthly averages and a 30-d running mean has been applied to the model results.

IGOSS Station	Location (Lat., Long.)	0.5° 1.5-Layer	0.5° 3.5-Layer	0.25° 3.5-Layer
Davao, Philippines	(07°05' N, 125°38' E)	0.68	0.66	0.68
Malakal, Belau	(07°20' N, 134°28' E)	0.40	0.46	0.43
Yap, F.S.M.	(09°31' N, 138°08' E)	0.36	0.26	0.32
Truk Moen, F.S.M.	(07°27' N, 151°51' E)	0.61	0.58	0.37
Kwajalein, Marshall Is.	(08°44' N, 167°44' E)	0.54	0.54	0.33
Tarawa, Kiribati	(01°22' N, 172°56' E)	0.31	0.52	0.53
Nauru, Nauru	(00°32' S, 166°54' E)	0.24	0.47	0.46
Rabaul, P.N.G.	(04°12' S, 152°11' E)	0.75	0.83	0.83
Penrhyn, Cook Island	(09°01' S, 158°04' W)	0.71	0.76	0.77
Honiara, Solomons	(09°26' S, 159°57' E)	0.74	0.73	0.82
Suva, Fiji	(18°08' S, 178°26' E)	0.58	0.67	0.56
Noumea, New Caledonia	(22°18' S, 166°26' E)	0.25	0.29	0.21
Midway, USA Trust	(28°13' N, 177°22' W)	-0.02	0.01	0.13
Honolulu, HI	(21°18' N, 157°52' W)	0.45	0.42	0.03
Neah Bay, WA	(48°22' N, 124°37' W)	0.85	0.86	0.86
Crescent City, CA	(41°45' N, 124°12' W)	0.67	0.71	0.75
San Francisco, CA	(37°48' N, 122°28' W)	0.57	0.61	0.61
San Diego, CA	(32°42' N, 117°10' W)	0.40	0.57	0.55
Isla Cedros, Mexico	(28°11' N, 115°13' W)	0.44	0.59	0.62
Cabo San Lucas, Mexico	(22°53' N, 109°54' W)	0.38	0.56	0.56
Puerto Vallarta, Mexico	(20°37' N, 105°15' W)	0.32	0.38	0.36
Acapulco, Mexico	(16°50' N, 99°55' W)	0.54	0.52	0.54
Salina Cruz, Mexico	(16°10' N, 95°12' W)	0.36	0.44	0.44
Buenaventura, Colombia	(03°54' N, 77°06' W)	0.56	0.56	0.57
Tumaco, Colombia	(01°50' N, 78°44' W)	0.63	0.63	0.66
La Libertad, Ecuador	(02°12' S, 80°55' W)	0.64	0.62	0.66
Callao, Peru	(12°03' S, 77°09' W)	0.66	0.70	0.70
Baltra, Ecuador	(00°26' S, 90°17' W)	0.62	0.57	0.57
Santa Cruz, Ecuador	(00°45' S, 90°19' W)	0.64	0.67	0.66

To determine the model response to interannual time scales, a 12-month running mean was applied to the model time series and to the IGOSS stations without long data gaps, and correlation coefficients were computed (not shown). For stations in the eastern Pacific, this correlation was higher at all locations than the values given in Table 3. The average correlation for the monthly time series was 0.61, but the average correlation for the 12-month running mean data was 0.82. The highest correlation was at Crescent City, CA, which reached 0.91. The stations in the western and central equatorial Pacific did not show this marked improvement in determining the interannual

variability from 1981 to 1989. The average correlations for the 12-month running mean data were nearly identical to the average correlations for the monthly data. Analysis showed that the later years (1988 and 1989) of the time series seemed to lower the interannual correlations. When recomputed over the 1981 to 1987 time frame, the average correlations of the 12-month running mean data for the western and central stations increased by approximately the same margin as was seen in the eastern Pacific stations.

This lowering of correlations by including time series after 1987 appears to result from an operational change to the ECMWF model/data assimilation in 1987, which increased the amplitude of the winds in the tropics. These results do not imply a decrease in the quality of the ECMWF winds due to the operational change. After an adjustment period, the observed and hindcast SSH time series appear to parallel each other at least as well as before the change. The decrease in correlation from including the period after the change results from the relative length of the time series before and after the change, and the strong signal of the 1982–83 El Niño in the time series.

## 8.0 CONCLUSIONS

The ability of the global reduced-gravity models to hindcast wind-driven anomalies has been documented by comparing model results with various observational data sets, including satellite altimetry, drifting buoys, and sea-level data. Three models that use various horizontal and vertical resolution were studied. Because these models omit the barotropic mode and are either non-eddy resolving or only marginally eddy resolving, they lack much of the mesoscale variability associated with the major western boundary currents. Due to this limitation, most comparisons were for wind-driven anomalies in the tropical latitudes. A technique was also developed to show regions where the SSH variability is deterministic (in response to atmospheric forcing) and nondeterministic (due to flow instabilities).

The generally good comparison of SSH anomalies between the model and the Geosat-ERM indicates that the model is accurately responding to the large-scale wind driving in the tropics, a result that owes credit to the ECMWF 1000-mbar winds as well. At the same time it adds credibility to the large-scale orbit error correction techniques used to process the altimetric data. On a finer scale, the models were able to represent the complex current structure of the western equatorial Pacific Ocean as indicated by comparisons with drifting buoys and ADCP data. Finally, the model's interannual variability of sea level at various tropical and midlatitude stations compares quite well with the observed data.

The greatest improvement in the model/data comparisons came when the vertical resolution was increased from 1.5 to 3.5 layers. This increase allows for the formation of the Equatorial Undercurrent and a much more realistic South Equatorial Current. Increasing the horizontal resolution from  $0.5^\circ$  to  $0.25^\circ$  improved the representation of the complex currents in the western equatorial Pacific, but did not significantly improve the comparisons at island/coastal sea-level stations. The success of these comparisons depended on a relatively direct ocean model response to atmospheric forcing. Increasing the resolution increased the fraction of the variability due to flow instabilities, which are not a direct response to atmospheric forcing. These flow instabilities tend to degrade comparisons aimed at the wind-driven response. However, it is obvious that even finer resolution and the barotropic mode are needed to accurately model the mesoscale variability due to flow instabilities in the midlatitude and subpolar regions of the world oceans (Hurlburt et al. 1992; Hogan et al. 1992).

## 9.0 ACKNOWLEDGMENTS

This work was performed as part of the Naval Research Laboratory 6.2/6.3 Global Ocean Prediction System projects. These are components of the Navy Ocean Modeling Program managed by Mr. Robert Peloquin, Office of Naval Research, under program elements 0602435N and 0603207N. It is also a contribution to the NRL 6.1 Eddy-Resolving Global Ocean Model project, managed by Dr. William Moseley, under program element 0601153N, sponsored by the Office of Naval Research. Thanks are extended to Dr. Phil Richardson for providing the analysis of WEPOCS III data and a ship drift climatology. The numerical simulations were performed on the Primary Oceanographic Prediction System CRAY Y-MP 8/8128 at the Naval Oceanographic Office.

## 10.0 REFERENCES

- Busalacchi, A. J., K. Takeuchi, and J. J. O'Brien, "On the Interannual Wind-Driven Response of the Tropical Pacific Ocean," in *Hydrodynamics of the Equatorial Ocean*, J. C. J. Nihoul, ed. (Elsevier Science Publishers, Amsterdam, 1983), pp. 155-195.
- Cane, M. A., S. E. Zebiak, and S. C. Dolan, "Experimental Forecasts of El Niño," *Nature* **321**, 827-832 (1986).
- Cheney, R. E., B. C. Douglas, R. W. Agreen, L. Miller, D. L. Porter, and N. S. Doyle, "Geosat Altimeter Geophysical Data Record User Handbook," NOS NGS-46, NOAA Tech. Memo, 1987.
- Gordon, A. L., "Interocean Exchange of Thermohaline Water," *J. Geophys. Res.* **91**, 5037-5046 (1986).
- Haines, B. J., G. H. Born, J. G. Marsh, and R. G. Williamson, "Precise Orbit Computation for the Geosat Exact Repeat Mission," *J. Geophys. Res.* **95**, 2871-2886 (1990).
- Haney, R. L., "A Numerical Case Study of the Development of Large-Scale Thermal Anomalies in the Central North Pacific Ocean," *J. Phys. Oceanogr.* **10**, 541-556 (1980).
- Hellerman, S. and M. Rosenstein, "Normal Monthly Wind Stress Over the World Ocean with Error Estimates," *J. Phys. Oceanogr.* **13**, 1093-1104 (1983).
- Hogan, P. J., H. E. Hurlburt, G. A. Jacobs, A. J. Wallcraft, W. J. Teague, and J. L. Mitchell, "Simulation of Geosat, TOPEX/POSEIDON, and ERS-1 Altimeter Data from a 1/8° Pacific Ocean Model: Effects of Space-Time Resolution on Mesoscale Sea Surface Height Variability," *J. Mar. Technol. Soc.* **26**(2), 98-107 (1992).
- Hurlburt, H. E., "The Potential for Ocean Prediction and the Role of Altimeter Data," *Mar. Geod.* **8**, 17-66 (1984).
- Hurlburt, H. E., "The Ocean Prediction Problem and its Diversity: Some Issues and Possible Solutions," in *Ocean Prediction Workshop 1986*, C. N. K. Mooers, A. R. Robinson, and J. D. Thompson, eds. (Oceanographer of the Navy, Washington, D.C., and Office of Naval Research, Arlington, VA, 1987), pp. 192-226.

- Hurlburt, H. E., J. C. Kindle, E. J. Metzger, and A. J. Wallcraft, "Results from a Global Model in the Western Tropical Pacific," in *Proceedings of the Western Pacific International Meeting and Workshop on TOGA COARE*, J. Picaut, R. Lukas, and T. Delcroix, eds. (Centre ORSTOM de Noumea, New Caledonia, 1989), pp. 343–354.
- Hurlburt, H. E. and J. D. Thompson, "A Numerical Study of Loop Current Intrusions and Eddy Shedding," *J. Phys. Oceanogr.* **10**, 1611–1651 (1980).
- Hurlburt, H. E., A. J. Wallcraft, Z. Sirkes, and E. J. Metzger, "Modeling of the Global and Pacific Oceans: On the Path to Eddy-Resolving Ocean Prediction," *Oceanography* **5**, 9–18 (1992).
- Jacobs, G. A., G. H. Born, M. E. Parke, and P. C. Allen, "The Global Structure of the Annual and Semiannual Sea Surface Height Variability from Geosat Altimeter Data," *J. Geophys. Res.* (C11), **97**, 17813–17828 (1992).
- Kindle, J. C., H. E. Hurlburt, and E. J. Metzger, "On the Seasonal and Interannual Variability of the Pacific to Indian Ocean Throughflow," in *Proceedings of the Western Pacific International Meeting and Workshop on TOGA COARE*, J. Picaut, R. Lukas, and T. Delcroix, eds. (Centre ORSTOM de Noumea, New Caledonia, 1989), pp. 355–365.
- Kindle, J. C. and P. A. Phoebus, "The Ocean Response to Operational Westerly Wind Bursts During 1991–92 El Niño," submitted to *J. Geophys. Res.* (in press) (1994).
- Levitus, S., "Climatological Atlas of the World Ocean," NOAA Professional Paper 13, Geophysical Fluid Dynamics Laboratory, Princeton, NJ, 1982, 173 pp.
- Levitus, S., unpublished data tapes for ship drift (1989).
- Lukas, R. and E. Firing, "The Geostrophic Balance of the Pacific Equatorial Undercurrent," *Deep-Sea Research* **31**, 61–66 (1984).
- Lukas, R., E. Firing, P. Hacker, P. Richardson, C. Collins, R. Fine, and R. Gammon, "Observations of the Mindanao Current During the Western Equatorial Pacific Ocean Circulation Study," *J. Geophys. Res.* **96**, 7089–7104 (1991).
- Ly, L. N., J. C. Kindle, J. D. Thompson, and W. J. Youtsey, "Wind Stress Analysis over the Western Equatorial Pacific and North Atlantic Oceans Based on ECMWF Operational Wind Products," Tech. Report TR-3, Inst. Naval Oceanog., 1992, 117 pp.
- Metzger, E. J., H. E. Hurlburt, J. C. Kindle, Z. Sirkes, and J. Pringle, "Hindcasting of Wind-Driven Anomalies Using a Reduced-Gravity Global Ocean Model," *J. Mar. Technol. Soc.* **26**(2), 23–32 (1992).
- Pares-Sierra, A. and J. J. O'Brien, "The Seasonal and Interannual Variability of the California Current System: A Numerical Model," *J. Geophys. Res.* **94**, 3159–3180 (1989).
- Philander, S. G., "El Niño, La Niña and the Southern Oscillation," International Geophysics Series, R. Dmowska and J. R. Holton, eds. (Academic Press, New York, 1990), Vol. 46, 293 pp.
- Richardson, P. L. and T. K. McKee, "Surface Velocity in the Equatorial Oceans (20° N–20° S) Calculated from Historical Ship Drifts," WHOI-89-9, Woods Hole Oceanog. Inst. Tech. Rept., 1989, 50 pp.

- Schmitz, W. J. and P. L. Richardson, "On the Sources of the Florida Current," *Deep-Sea Res.* **38**, S379–S409 (1991).
- Teague, W. J. and P. J. Hogan, "Regional Plots from the GDEM and Levitus Climatologies," NORDA Technical Note 361, Naval Research Laboratory, Stennis Space Center, MS, 1989.
- Wallcraft, A. J., "The Navy Layered Ocean Model Users Guide," NOARL Report 35, Naval Research Laboratory, Stennis Space Center, MS, 1991.
- Wyrtki, K., "Physical Oceanography of the Southeast Asian Waters," NAGA Report 2, Scripps Inst. Oceanogr., 1961, 195 pp.
- Wyrtki, K. and B. Kilonsky, "Mean Water and Current Structure During the Hawaii-to-Tahiti Shuttle Experiment," *J. Phys. Oceanogr.* **14**, 242–254 (1984).
- Zlotnicki, V., L.-L. Fu, and W. Patzert, "Seasonal Variability in Global Sea Level Observed with Geosat Altimetry," *J. Geophys. Res.* **94**, 17959–17969 (1989).